WiBall: A Time-Reversal Focusing Ball Method for Decimeter-Accuracy Indoor Tracking

Feng Zhang, *Student Member, IEEE*, Chen Chen, *Student Member, IEEE*, Beibei Wang, *Senior Member, IEEE*, Hung-Quoc Lai, Yi Han, and K. J. Ray Liu, *Fellow, IEEE*

***Abstract*—With the development of the Internet of Things technology, indoor tracking has become a popular application nowadays, but most existing solutions can only work in line-of-sight scenarios, or require regular recalibration. In this paper, we propose WiBall, an accurate and calibration-free indoor tracking system that can work well in non-line-of-sight based on radio signals. WiBall leverages a stationary and location-independent property of the time-reversal focusing effect of radio signals for highly accurate moving distance estimation. Together with the direction estimation based on inertial measurement unit and location correction using the constraints from the floorplan, WiBall is shown to be able to track a moving object with decimeter-level accuracy in different environments. Since WiBall can accommodate a large number of users with only a single pair of devices, it is low-cost and easily scalable, and can be a promising candidate for future indoor tracking applications.**

***Index Terms*—Indoor tracking, radio signals, speed estimation, time-reversal transmission.**

I. Introduction

With the proliferation of the Internet of Things applications, indoor positioning and indoor navigation (IPIN) has received an increasing attention in recent years. Technavio forecasts the global IPIN market to grow to \$7.8 billion by 2021 [1], and more than ever before, enterprises of all sizes are investing in IPIN technology to support a growing list of applications, including patient tracking in hospitals, asset management for large groceries, workflow automation in large factories, navigation in malls, appliance control, etc.

Although global positioning system can achieve good accuracy with a low cost in outdoor real-time tracking, such a good balance between the cost and performance has not been realized for indoor tracking yet [2].

Manuscript received December 12, 2017; revised June 7, 2018; accepted July 1, 2018. Date of publication July 10, 2018; date of current version November 14, 2018. *(Corresponding author: Feng Zhang.)*

F. Zhang, B. Wang, and K. J. R. Liu are with the Department of Electrical and Computer Engineering, University of Maryland at College Park, College Park, MD 20742 USA, and also with the R&D Department, Origin Wireless, Inc., Greenbelt, MD 20770 USA (e-mail: fzhang15@umd.edu; bebewang@umd.edu; kjrliu@umd.edu).

C. Chen was with the Department of Electrical and Computer Engineering, University of Maryland at College Park, College Park, MD 20742 USA, and was also with the R&D Department, Origin Wireless Inc., Greenbelt, MD 20770 USA. He is now with Pinterest, Inc., San Francisco, CA 94103-4904 USA (e-mail: cc8834@umd.edu).

H.-Q. Lai and Y. Han are with the R&D Department, Origin Wireless, Inc., Greenbelt, MD 20770 USA (e-mail: quoc.lai@originwireless.net; yi.han@originwireless.net).

Digital Object Identifier 10.1109/JIOT.2018.2854825

In this paper, we propose WiBall, a wireless system for indoor tracking, that can work well in both non-line-of-sight (NLOS) and line-of-sight (LOS) scenarios and is robust to environmental dynamics as well. WiBall estimates the incremental displacement of the device at every moment, and thus, it can track the trace of the device in real time. WiBall adopts a completely new paradigm in the moving distance estimation, which is built on the proposed discovered physical phenomenon of radio signals. In the past, the moving distance estimation can be done by analyzing the output of IMU that is attached to the moving object. Accelerometer readings are used to detect walking steps and then, the walking distance can be estimated by multiplying the number of steps with the stride length [3]. However, pedestrians often have different stride lengths that may vary up to 40% even at the same speed, and 50% with various speeds of the same person [4]. Thus, calibration is required to obtain the average stride lengths for different individuals, which is impractical in real applications and thus has not been widely adopted. The moving distance can also be estimated by analyzing radio signals that are affected by the movement of the device. Various methods have been proposed based on the estimation of the maximum Doppler frequency, such as level crossing rate methods [5], covariance-based methods [6], [7], and wavelet-based methods [8]. However, the performance of these estimators is unsatisfactory in practical scenarios. For example, the approach in [7] can only differentiate whether a mobile station moves with a fast speed ($\geq$ 30 km/h) or with a slow speed ($\leq$ 5 km/h).

In WiBall, a new scheme for moving distance estimation based on the time-reversal (TR) resonating effect [9], [10] is proposed. TR is a fundamental physical resonance phenomenon that allows people to focus the energy of a transmitted signal at an intended focal spot, both in the time and spatial domains, by transmitting the TR waveform. The research of TR can be traced back to the 1950s when it was first utilized to align the phase differences caused by multipath fading during long-distance information transmissions. The TR resonating effect was first observed in a practical underwater propagation environment [11] that the energy of a transmitted signal can be refocused at the intended location because by means of TR the RX recollects multipath copies of a transmitted signal in a coherent matter.

In this paper, we present a new discovery that the energy distribution of the TR focusing effect exhibits a location-independent property, which is only related to the physical

2327-4662 © 2018 IEEE. Personal use is permitted, but republication/redistribution requires IEEE permission.
See http://www.ieee.org/publications_standards/publications/rights/index.html for more information.

parameters of the transmitted EM waves. This is because the number of multipath components (MPCs) in indoors is so large that the randomness of the received energy at different locations can be averaged out as a result of the law of large numbers. Based on this location-independent feature, WiBall can estimate the moving distance of the device in a complex indoor environment without requiring any precalibration procedures. To cope with the cumulative errors in distance estimation, WiBall incorporates the constraints imposed by the floorplan of buildings and corrects the cumulative errors whenever a landmark, such as a corner, hallway, door, etc., is met. Combining the improved distance estimator and the map-based error corrector, the proposed WiBall is shown to be able to achieve decimeter-level accuracy in real-time tracking regardless of the moving speed and environment.

The rest of this paper is organized as follows. Section II introduces the related works. Section III introduces the system architecture of WiBall followed by a discussion on the TR principle for distance estimation. Section IV presents an IMU-based moving direction estimator and a map-based localization corrector, which can correct the accumulated localization error. Experimental evaluation is shown in Section V and Section VI concludes this paper.

II. Related Works

Existing solutions for indoor tracking can be classified into four categories: 1) vision-based; 2) audio-based; 3) radio-based; and 4) inertial measurement unit (IMU)-based. Vision-based approaches, such as camera [12], laser [13], infrared [14], etc., suffer from high cost of deployment and equipment, sophisticated calibrations and limited coverage, although a very high accuracy can be achieved. The acoustic-based schemes [15] can only cover a limited range and are not scalable to a large number of users. The performance of radio-based approaches, such as RADAR [16], RFID [17], and UWB localization systems [18], [19], is severely affected by the NLOS multipath propagation which is unavoidable for a typical indoor environment. The localization accuracy of IMU-based methods [3], [4] is mainly limited by the poor estimation of moving distance and the drifting of the gyroscope.

Due to the wide deployment of WiFi in indoors, various indoor localization systems based on WiFi have been proposed, as summarized in Table I. In general, these works can be classified into two categories: 1) modeling-based approach and 2) fingerprinting-based approach. The features utilized in these approaches can be obtained either from the MAC layer information, e.g., receive signal strength indicator (RSSI) readings and the timestamps of the received packets at the receiver (RX), or from the PHY information, e.g., the channel state information (CSI).

In the modeling-based schemes, either the distance [20]–[23], or the angle [24]–[26] between an anchor point and the device can be estimated and the device can be localized by performing geometrical triangulation. The distance between the anchor point and the device can be estimated from the decay of RSSI [27] or from the time of arrival (ToA) of the transmitted packets which can be extracted from

TABLE I
Brief Summary of Typical WiFi-Based Approaches

	Method	Existing Solutions
Modeling-based	ToA	CAESAR [20], ToneTrack [28]
	AoA	ArrayTrack [36], SpotFi [24], Phaser [25]
	RSSI	RADAR [22]
	CSI	FILA [37]
Fingerprinting-based	RSSI	Horus [27], Nibble [32]
	CSI	PinLoc [38], TRIPS [35], DeepFi [33]

the timestamps of the received packets [28]. The angle in between can be obtained by examining the features of the CSI received by multiple receive antennas, and then, the angle of arrival (AoA) of the direct path to the target can be calculated. ToA-based methods typically require synchronization between the anchor point and the device and thus are very sensitive to timing offsets [29]; AoA-based methods require an array of phased antennas which are not readily available in commercial WiFi chips [25]. Recently, a decimeter-level tracking system, Widar, is proposed in [30] and [31], however, the system can only work in a small area with the constraint of LOS. The main challenges for the modeling-based approaches are the blockage and reflection of the transmitted signal since only the signal coming from the direct path between the anchor point and the device is useful for localization.

The fingerprinting-based schemes consist of an offline phase and an online phase. During the offline phase, features associated with different locations are extracted from the WiFi signals and stored in a database; in the online phase, the same features are extracted from the instantaneous WiFi signals and compared with the stored features so as to classify the locations. The features can be obtained either from the vector of RSSIs [27], [32], or the detailed CSI [33]–[35] from a specific location to all the anchor points in range. A major drawback of the fingerprinting-based approaches lies in that the features they use are susceptible to the dynamics of the environment. For example, the change of furniture or the status of doors may have a severe impact on these features and the database of the mapped fingerprints need to be updated before it can be used again. In addition, the computational complexity of the fingerprinting-based approaches scales with the size of the database and thus they are not feasible for low-latency applications, especially when the number of the collected fingerprints is large.

In sum, the performance of most existing solutions for indoor localization degrades dramatically under NLOS conditions, which are common usage scenarios though. Even with a significant overhead in the manual construction of the database, the fingerprinting-based approaches still fail to achieve a decimeter-level accuracy. Therefore, indoor location-based services are not provided as widespread as expected nowadays, which motivates us to design a highly accurate and robust indoor tracking system even without requiring specialized infrastructure.

III. TR Focusing Ball Method for Distance Estimation

In this section, we first introduce the overall system architecture of WiBall and the TR radio system. Then, we derive the analytical normalized energy distribution of the TR focal spot.

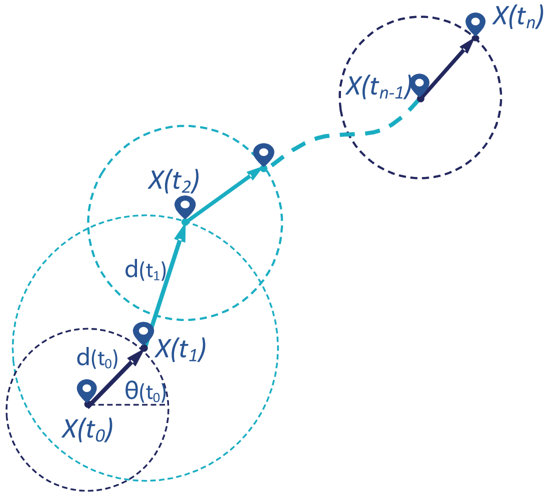

Fig. 1. Illustration of the tracking procedure.

We show that the normalized energy distribution is location-independent and can be used to estimate distance. Last, we discuss the TR-based distance estimator.

A. Overview of WiBall

WiBall consists of a transmitter (TX) broadcasting beacon signals periodically to all the RXs being tracked. WiBall estimates the paths that the RX travels, i.e., the location of the RX $\vec{\mathbf{x}}$ at time t_i is estimated as

$$\vec{\mathbf{x}}(t_i) = \vec{\mathbf{x}}(t_{i-1}) + \vec{\Delta}(t_i) \tag{1}$$

where $\vec{\mathbf{x}}(t_{i-1})$ represents the location of the RX at the previous time t_{i-1} and $\Delta(t_i)$ is the incremental displacement. The magnitude of $\vec{\Delta}(t_i)$, denoted as $d(t_i)$, and the angle of $\vec{\Delta}(t_i)$, denoted as $\theta(t_i)$, correspond to the moving distance and the change of moving direction of the RX from t_{i-1} to t_i, respectively. As shown in Fig. 1, the location of the RX at time t_n is computed based on the accumulative displacements from time t_0 to t_n and the initial start point $\vec{\mathbf{x}}(t_0)$.

WiBall estimates the moving distance $d(t_i)$ based on the TR resonating effect, which can be obtained from the CSI measurements at the RX. The estimation of $\theta(t_i)$ is based on the angular velocity and gravity direction from IMU, which is a built-in module for most smartphones nowadays.

B. TR Radio System

Consider a rich-scattering environment, e.g., an indoor or metropolitan area, and a wireless transceiver pair each equipped with a single omnidirectional antenna. Given a large enough bandwidth, the MPCs in a rich-scattering environment can be resolved into multiple taps in discrete-time and let $h(l; \vec{T} \rightarrow \vec{R}_0)$ denote the lth tap of the channel impulse response (CIR) from $\vec{T}$ to $\vec{R}_0$, where $\vec{T}$ and $\vec{R}_0$ denotes the coordinates of the TX and RX, respectively. In the TR transmission scheme, the RX at $\vec{R}_0$ first transmits an impulse and the TX at $\vec{T}$ captures the CIR from $\vec{R}_0$ to $\vec{T}$. Then the RX at $\vec{T}$ simply transmits back the time-reversed and conjugated version of the captured CIR, i.e., $h^*(-l; \vec{R}_0 \rightarrow \vec{T})$, where $*$ denotes complex conjugation. With channel reciprocity, i.e., the forward and

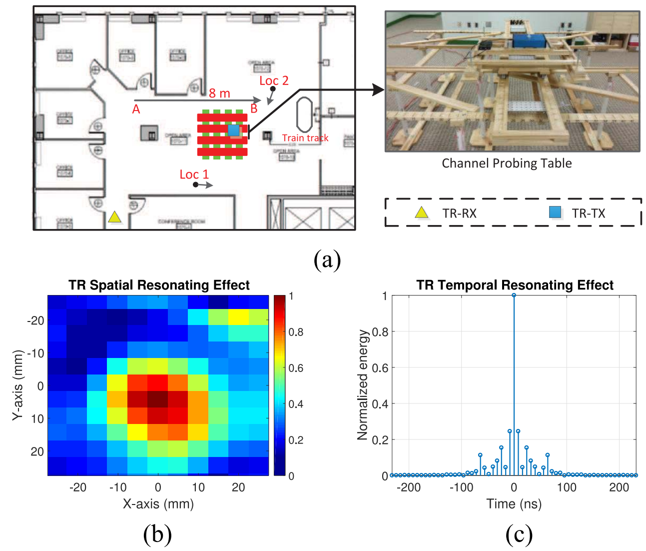

Fig. 2. TR prototype and the environment of the measurement, the TRRS distribution in the spatial domain, and the normalized energy of the received signal at the focal spot $\vec{R}_0$ in the time domain. (a) TR prototype and channel probing platform. (b) TRRS in spatial domain. (c) TRRS in time domain.

backward channels are identical [35], the received signal at any location $\vec{R}$ when the TR waveform $h^*(-l; \vec{R}_0 \rightarrow \vec{T})$ is transmitted can be written as [39]

$$s(l; \vec{R}) = \sum_{m=0}^{L-1} h\big(m; \vec{T} \rightarrow \vec{R}\big) h^*\big(m - l; \vec{R}_0 \rightarrow \vec{T}\big) \tag{2}$$

where L is the number of resolved multipaths in the environment. When $\vec{R} = \vec{R}_0$ and $l = 0$, we have $s(0; \vec{R}) = \sum_{m=0}^{L-1} |h(m, \vec{T} \rightarrow \vec{R}_0)|^2$ with all MPCs added up coherently, i.e., the signal energy is refocused at a particular spatial location at a specific time instance. This phenomenon is termed as the TR spatial-temporal resonating effect [40], [41].

To study the TR resonating effect in the spatial domain, we fix time index $l = 0$ and define the TR resonating strength (TRRS) between the CIRs of two locations $\vec{R}_0$ and $\vec{R}$ as the normalized energy of the received signal when the TR waveform for location $\vec{R}_0$ is transmitted

$$\eta\big(\mathbf{h}(\vec{R}_0), \mathbf{h}(\vec{R})\big) = \left| \frac{s(0; \vec{R})}{\sqrt{\sum_{l_1=0}^{L-1} |h(l_1; \vec{T} \rightarrow \vec{R}_0)|^2} \sqrt{\sum_{l_2=0}^{L-1} |h\big(l_2; \vec{T} \rightarrow \vec{R}\big)|^2}} \right|^2 \tag{3}$$

where we use $\mathbf{h}(\vec{R})$ as an abbreviation of $h(l; \vec{T} \rightarrow \vec{R})$, $l = 0, \ldots, L-1$, when $\vec{T}$ is fixed. Note that the range of TRRS is normalized to be [0, 1] and TRRS is symmetric, i.e., $\eta(\mathbf{h}(\vec{R}_0), \mathbf{h}(\vec{R})) = \eta(\mathbf{h}(\vec{R}), \mathbf{h}(\vec{R}_0))$.

We built a pair of customized TR devices to measure the TRRS at different locations, as shown in Fig. 2(a). The devices operate at $f_0 = 5.8$ GHz ISM band with 125 MHz bandwidth, and the corresponding wavelength is $\lambda = c/f_0 = 5.17$ cm. The RX is placed on a 5 $\times$5 cm square area above a channel probing table with 0.5 cm resolution, and the center of the square is set to be the focal spot $\vec{R}_0$. The TRRS distribution around $\vec{R}_0$

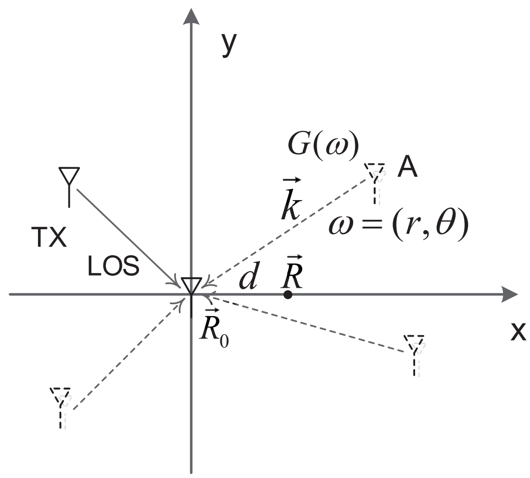

Fig. 3. Illustration of the polar coordinates in the analysis.

in the spatial domain and the normalized received energy at $\vec{R}_0$ in the time domain are shown in Fig. 2(b) and (c), respectively. As we can see from the results, the received energy is concentrated around $\vec{R}_0$ both in spatial and time domains almost symmetrically, which shows that a bandwidth of 125 MHz is able to achieve the TR resonating effect in a typical indoor environment.

C. Energy Distribution of TR Focal Spot

Assume that all the EM waves propagate in a far-field zone, and then each MPC can be approximated by a plane EM wave. For the purpose of illustration, the receive antenna is placed in the origin of the space and each MPC can be represented by a point in the space whose coordinate is determined by its AoA and propagation distance, e.g., the point A, as shown in Fig. 3, where r stands for the total traveled distance of the MPC, θ denotes the direction of arrival of the MPC, and $G(\omega)$ denotes the power gain with $\omega = (r, \theta)$. In a rich-scattering environment, we can also assume that ω is uniformly distributed in the space and the total number of MPCs is large. When a vertically polarized antenna is used, only the EM waves with the direction of electric field orthogonal to the horizontal plane are collected. Then, the received signal is just a scalar sum of the electric field of the impinging EM waves along the vertical direction. In the sequel, without loss of generality, we only consider the TRRS distribution in the horizontal plane since its distribution in the vertical plane is similar.

For a system with bandwidth B, two MPCs would be divided into different taps of the measured CIR as long as the difference of their ToA is larger than the sampling period $1/B$, that is, any two MPCs with a difference of their traveled distances larger than c/B can be separated. With a sufficiently large system bandwidth B, the distance resolution c/B of the system is so small that all of the MPCs with significant energy can be separated in the spatial domain, i.e., each significant MPC can be represented by a single tap of a measured CIR. Assume that the distribution of the energy of each MPC is uniform in direction θ, i.e., the distribution of $G(\omega)$ is only a function of r. Then the energy of MPCs coming from different directions would be approximately the same when the number of MPCs is large. Mathematically, for any point $\vec{R}$ in a source-free region with constant mean electric and magnetic fields, the CIR when a delta-like pulse is transmitted can be written as [39]

$$h\left(t; \vec{T} \to \vec{R}\right) = \sum_{\omega \in \Omega} G(\omega) q(t - \tau(\omega)) e^{i\left(2\pi f_0 (t - \tau(\omega)) - \phi(\omega) - \vec{k}(\omega) \cdot \vec{R}\right)} \quad (4)$$

where $q(t)$ is the pulse shaper, $\tau(\omega) = r/c$ is the propagation delay of the MPC ω, f_0 is the carrier frequency, Ω is the set of MPCs, $\phi(\omega)$ is the change of phase due to reflections, and $\vec{k}(\omega)$ is the wave vector with amplitude $k = c/f_0$. Accordingly, the lth tap of a sampled CIR at location $\vec{R}$ can be expressed as

$$h\left(l; \vec{T} \to \vec{R}\right) = \sum_{\tau(\omega) \in \left[lT - \frac{T}{2}, lT + \frac{T}{2}\right)} G(\omega) q(\Delta\tau(l, \omega)) e^{i\left(2\pi f_0 \Delta\tau(l,\omega) - \phi(\omega) - \vec{k}(\omega) \cdot \vec{R}\right)} \quad (5)$$

where T is the channel measurement interval and $\Delta\tau(l, \omega) = lT - \tau(\omega)$ for $l = 0, 1, \ldots, L-1$. When the TR waveform $h^*(-l; \vec{R}_0 \to \vec{T})$ is transmitted, the corresponding received signal at the focal spot $\vec{R}_0$ can be written as

$$s\left(0; \vec{R}\right) = \sum_{l=1}^{L} \left| \sum_{\tau \in \left[lT - \frac{T}{2}, lT + \frac{T}{2}\right)} G(\omega) q(\Delta\tau(l, \omega)) e^{i(2\pi f_0 \Delta\tau(l,\omega) - \phi(\omega))} \right|^2. \quad (6)$$

Equation (6) shows that the MPCs with propagation delays $\tau(\omega) \in [lT - (T/2), lT + (T/2))$ for each l would be merged into one single tap, and the signals coming from different taps would add up coherently while the MPCs within each sampling period T would add up incoherently. It indicates that the larger the bandwidth, the larger the TR focusing gain that can be achieved, since more MPCs can be aligned and added up coherently. When the bandwidth is sufficiently large, the received signal at each point $\vec{R}$ can be approximated as

$$s\left(0; \vec{R}\right) \approx \sum_{l=1}^{L} |G(\omega) q(\Delta\tau(l, \omega))|^2 e^{-i\vec{k}(\omega) \cdot \left(\vec{R} - \vec{R}_0\right)}. \quad (7)$$

When a rectangular pulse shaper is used, i.e., $q(t) = 1$ for $t \in [-(T/2), (T/2))$ and $q(t) = 0$ otherwise, under the above symmetric scattering assumption the received signal $s(0; \vec{R})$ can thus be approximated as

$$\begin{aligned} s\left(0; \vec{R}\right) &= \sum_{\omega \in \Omega} |G(\omega)|^2 e^{-i\vec{k} \cdot \left(\vec{R} - \vec{R}_0\right)} \\ &\approx \int_0^{2\pi} P(\theta) e^{-ikd\cos(\theta)} d\theta \\ &= P J_0(kd) \end{aligned} \quad (8)$$

where the coordinate system in Fig. 3 is used, Ω stands for the set of all significant MPCs, $J_0(x)$ is the zeroth-order Bessel function of the first kind, and d is the Euclidean distance between $\vec{R}_0$ and $\vec{R}$. Here we use a continuous integral

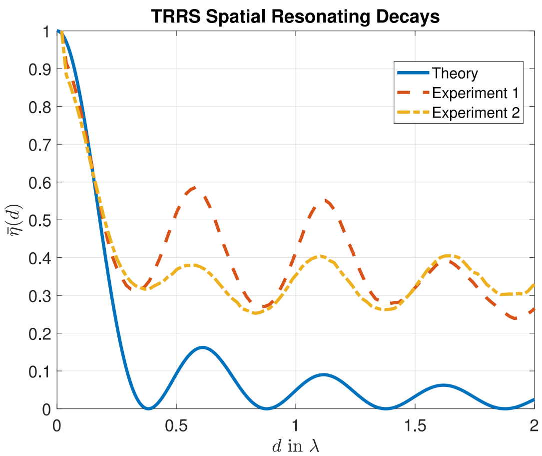

(a)

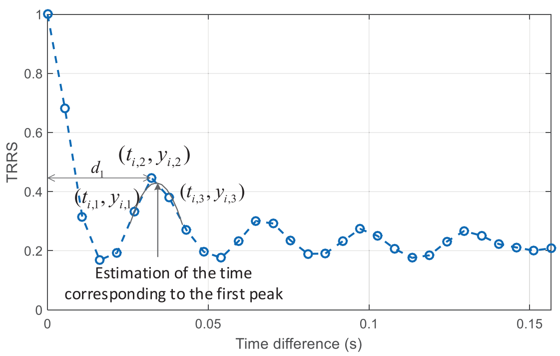

(b)

Fig. 4. Distributions of TRRS. (a) Comparison of the TRRS distribution between experimental results and the theoretical result. Experiments 1 and 2 correspond to Location 1 and Location 2, respectively, in Fig. 2(a). (b) Illustration of the proposed TR-based speed estimation algorithm.

to approximate the discrete sum and $P(\theta) = P$ denotes the density of the energy of MPCs coming from direction θ. For $\vec{R} = \vec{R}_0$, it degenerates to the case of $d = 0$ and thus $s(0; \vec{R}_0) \approx P$. Since the denominator of (3) is the product of the energy received at two focal spots, it would converge to P^2. At the same time, the numerator is approximately $P^2 J_0^2(kd)$ as discussed above. As a result, the TRRS defined in (3) can be approximated as

$$\eta\big(\mathbf{h}(\vec{R}_0), \mathbf{h}(\vec{R})\big) \approx J_0^2(kd). \quad (9)$$

In the following, since the theoretic approximation of the TRRS distribution only depends on the distance between two points, we use $\bar{\eta}(d) = J_0^2(kd)$ to stand for the approximation of TRRS between two points with distance d.

To evaluate the above theoretic approximation, we also built a mobile channel probing platform equipped with stepping motors that can control the granularity of the CIR measurements precisely along any predefined direction. Extensive measurements of CIRs from different locations have been collected in the environment shown in Fig. 2(a). Fig. 4(a) shows two typical experimental results measured at Location 1 and Location 2 with a separation of 10 m as shown in Fig. 2(a). The distance d away from each predefined focal spot increases from 0 to 2λ with a resolution of 1 mm. The measured TRRS

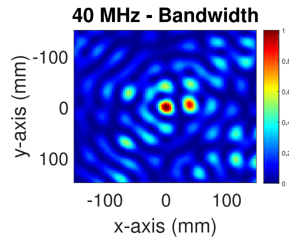

(a)

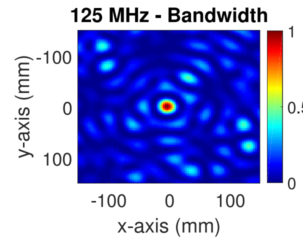

(b)

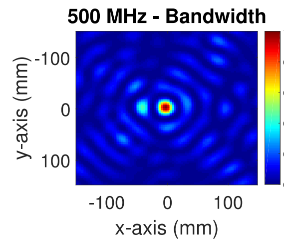

(c)

Fig. 5. Numerical simulations of the distributions of TRRS with varying bandwidth. (a) 40 MHz bandwidth. (b) 125 MHz bandwidth. (c) 500 MHz bandwidth.

distribution functions agree with the theoretic approximation quite well in the way that the positions of the peaks and valleys in the measured curves are almost the same as those of the theoretic curve. Although Locations 1 and 2 are far apart, the measured TRRS distribution functions exhibit similar damping pattern when the distance d increases.

We also observe that the measured TRRS distribution functions are far above 0. This is due to the contribution of the direct path between the TR devices. Therefore, the energy density function $P(\theta)$ in (8) consists of a term which is symmetric in direction due to NLOS components and another term which is asymmetric in direction due to LOS components. As a result, the TRRS is indeed a superposition of $J_0^2(kd)$ and some unknown function which is the result of the asymmetric normalized energy distribution of MPCs in certain directions. Since the pattern of $J_0^2(kd)$, embedded in the TRRS distribution function, is location-independent, we can exploit this feature for speed estimation.

A numerical simulation using a ray-tracing approach is also implemented to study the impact of bandwidth on TRRS distribution. In the simulation, the carrier frequency of the transmitted signals is set to be 5.8 GHz. Two hundred scatterers are uniformly distributed in a 7.5 by 7.5 m square area. The reflection coefficient is distributed uniformly and independently in $(0, 1)$ for each scatterer. The distance between the TX and RX is 30 m and the RX (focal spot) is set to be the center of the square area. Fig. 5 shows the distributions of TRRS around the focal spot when the system bandwidth 40 MHz, 125 MHz, and 500 MHz, respectively. As we can see from the results, as the bandwidth increases, the distribution of TRRS in the horizontal plane becomes more deterministic-like and converges to the theoretical approximations.

D. TR-Based Distance Estimator

Since the shape of the TRRS distribution function $\bar{\eta}(d) \approx J_0^2(kd)$ is only determined by the wave number k which is

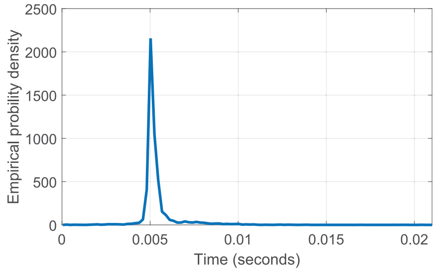

Fig. 6. Empirical probability density for time intervals between adjacent packets.

independent of specific locations, it can be utilized as an intrinsic ruler to measure distance in the space. Consider that an RX moves along a straight line with a constant speed v starting from location $\vec{R}_0$, and a TX keeps transmitting the TR waveform corresponding to $\vec{R}_0$ at regular intervals. Then, the TRRS measured at the RX is just a sampled version of $\eta(d)$, which would also exhibit the Bessel-function-like pattern, as illustrated in Fig. 4(b).

Take the first local peak of $\eta(d)$ for example. The corresponding theoretical distance d_1 is about 0.61λ according to the Bessel-function-like pattern. In order to estimate the moving speed, we only need to estimate how much time $\hat{t}$ it takes for the RX to reach the first local peak starting from point $\vec{R}_0$. We use a quadratic curve to approximate the shape of the first local peak. Combining the knowledge of the timestamps of each CIR measurement, $\hat{t}$ can be estimated by the vertex of the quadratic curve. Therefore, we obtain the speed estimation as $\hat{v} = (0.61\lambda)/\hat{t}$, and then, the moving distance can be calculated by integrating the instantaneous speed over time. One thing to note is that as long as the rate of CIR measurement is fast enough, it is reasonable to assume that the moving speed is constant during the measurement of the TRRS distribution. For example, in Fig. 4(b) the duration is about 0.16 s.

In practice, the channel is not measured with a uniform interval and the empirical probability density function of the time interval between adjacent channel measurements is shown in Fig. 6. To overcome the imperfect channel sampling process, we combine multiple realizations of the TRRS distribution function measured at adjacent time slots to increase the accuracy of the estimation of $\hat{t}$. For the ith measurement, first find the data points near the first local peak $(t_{i,j}, y_{i,j})$, $i = 1, \ldots, N$, $j = 1, 2, 3$, as shown in Fig. 4(b), where N is the number of TRRS distribution functions obtained within the window of channel measurements. Then fit the data points with a quadratic regression model $y_{i,j} = \alpha + \beta t_{i,j} + \gamma t_{i,j}^2 + e_{i,j}$, and thus estimation of the elapsed time is $\hat{t} = -\hat{\beta}_{\mathrm{LS}}/(2\hat{\gamma}_{\mathrm{LS}})$, where $\hat{\beta}_{\mathrm{LS}}$ and $\hat{\gamma}_{\mathrm{LS}}$ are the least-square estimators of β and γ, respectively. Different reference points can be used as well, such as the first local valley, the second local peak, and so on, to increase the accuracy of estimation. Therefore, the moving distance at time t can be estimated as $\hat{d}(t) = \hat{v}(t)\Delta t$, where Δt denotes the time duration between the current packet and the previous packet. The procedures of the proposed TR-based distance estimator has been summarized in the flowchart shown in Fig. 7.

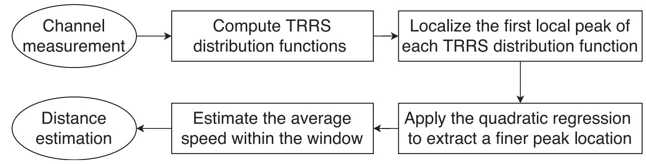

Fig. 7. Flowchart of the TR-based distance estimator.

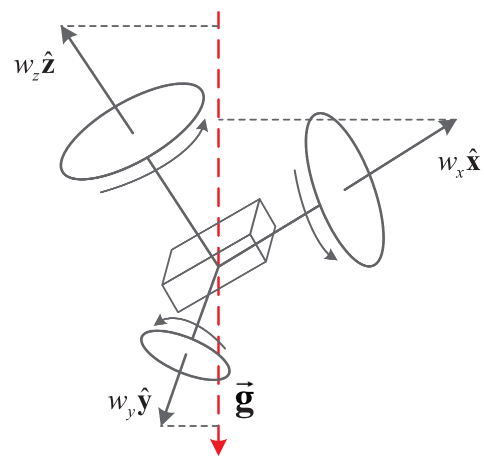

Fig. 8. Transforming the rotation of RX into the moving direction in horizontal plane.

Note that besides taking advantage of TR spatial focusing effect, the proposed distance estimator also exploits the physical properties of EM waves and thus does not require any precalibration, while the estimator presented in our previous work [40] needs to measure the TRRS spatial decay curve in advance.

IV. Moving Direction Estimation and Error Correction

In this section, we introduce the other two key components of WiBall: 1) the IMU-based moving direction estimator and 2) the map-based position corrector.

A. IMU-Based Moving Direction Estimator

If the RX is placed in parallel to the horizontal plane, the change of moving direction can be directly measured by the readings of the gyroscope in the z-axis, i.e., $\theta(t_i) = \omega_z(t_{i-1})(t_i - t_{i-1})$, where $\omega_z(t_{i-1})$ denotes the angular velocity of the RX with respect to z-axis in its local coordinate system at time slot t_{i-1}. However, in practice, the angle of the inclination between the RX and the horizontal plane is not zero, as shown in Fig. 8, and WiBall needs to transform the rotation of the RX into the change of the moving direction in the horizontal plane. Since the direction of the gravity $\vec{\mathbf{g}}/\|\vec{\mathbf{g}}\|$ can be estimated by the linear accelerometer, the rotation of the RX in the horizontal plane, which is orthogonal to the $\vec{\mathbf{g}}/\|\vec{\mathbf{g}}\|$, can be obtained by projecting the angular velocity vector $\vec{\boldsymbol{\omega}} = \omega_x\hat{\mathbf{x}} + \omega_y\hat{\mathbf{y}} + \omega_z\hat{\mathbf{z}}$ with respect to its local coordinate system onto the direction $\vec{\mathbf{g}}/\|\vec{\mathbf{g}}\|$. Therefore, the change

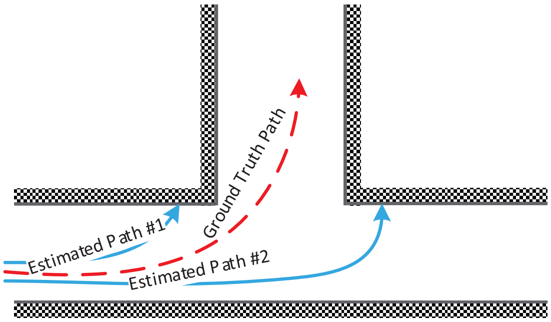

Fig. 9. Two possible estimated paths and the ground truth path.

of moving direction $\theta(t_i)$ is obtained as

$$\theta(t_i) = \frac{\vec{\boldsymbol{\omega}}^T(t_{i-1})\vec{\mathbf{g}}(t_{i-1})}{\|\vec{\mathbf{g}}(t_{i-1})\|} \cdot (t_i - t_{i-1}) \tag{10}$$

where $\vec{\boldsymbol{\omega}}(t_{i-1})$ and $\vec{\mathbf{g}}(t_{i-1})$ denote the vector of angular velocity and the gravity at time t_{i-1}, respectively.

B. Map-Based Position Corrector

Since WiBall estimates the current location of the RX based on the previous locations, its performance is limited by the cumulative error. However, for typical indoor environments, there are certain constraints in the floorplan which can be utilized as landmarks and thus, the cumulative errors may be corrected correspondingly as long as a landmark is identified. For example, Fig. 9 shows a T-shaped corridor and two possible estimated paths are illustrated in the figure. The moving distance of path #1 is underestimated and that of path #2 is overestimated, while the dotted line corresponds to the ground truth path. Both of the estimated traces would penetrate the wall in the floorplan if the errors are not corrected, which violates the physical constraints imposed by the structure of the building. In these two cases, a reasoning procedure can be implemented and WiBall tries to find the most possible path that can be fitted to the floorplan where all the border constraints imposed by the floorplan are satisfied. Therefore, the cumulative errors of both the distance estimations and direction estimations can be corrected when a map-based position correction is implemented.

V. Performance Evaluation

To evaluate the performance of WiBall, various experiments are conducted in different indoor environments using the prototype as shown in Fig. 2(a). In this section, we first evaluate the performance of the TR-based distance estimator. Then, the performance of WiBall in tracking a moving object in two different environments is studied. At last, the impact of packet loss and system window length on the proposed system is also discussed.

A. Evaluations of TR Distance Estimator

The first experiment is to estimate the moving distance of a toy train running on a track. We put one RX on a toy train as shown in Fig. 10(a) and place one TX about 20 m from the RX with two walls between them. The sampling period between adjacent channel measurement is set to $T = 5$ ms. CIRs are collected continuously when the toy train is running on the track. We also set an anchor point as shown in Fig. 10(a) on the train track and collect the CIR when the train is at the anchor. The TRRS values between all the measured CIRs and the CIR of the anchor are computed and shown in Fig. 10(b). The peaks in the red line indicate that the train passes the anchor three times. The estimated length of the track for this single loop is 8.12 m and the error is 1.50%, given the actual length of the train track is 8.00 m. The train slows down when it makes turns due to the increased friction and then speeds up in the straight line. This trend is reflected in the speed estimation shown by the blue curve. To show the consistency of the distance estimator over time, we collect the CIRs for 100 laps in total and estimate the track length for each lap separately. The histogram of the estimation results is shown in Fig. 11. The mean of the estimation error is about 0.02 m and the standard error deviation is about 0.13 m, which shows that the estimation is consistent even over a long period.

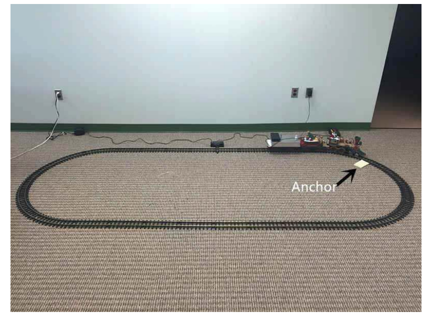

(a)

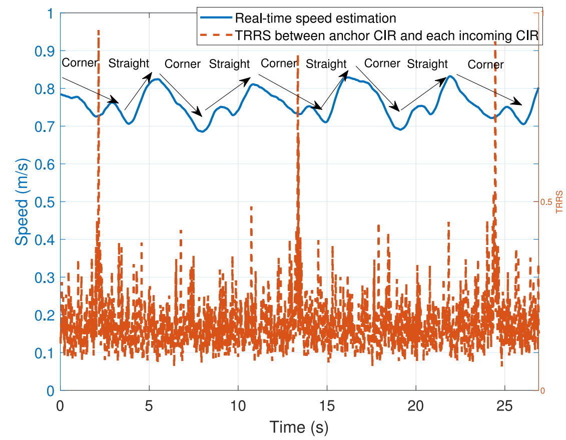

(b)

Fig. 10. Tracking the speed of the toy train. (a) Toy train and the train track used in the experiment. (b) Estimated speed of the toy train over time.

The second experiment is to estimate the human walking distance. One RX is put on a cart and one participant pushes the cart along the line from point A to point B shown in Fig. 2(a) with an approximately constant speed of 1 m/s. To control the walking speed, the participant uses a timer and landmarks placed on the floor during the experiment. In the upper panel of Fig. 12(a), for each time t, the TRRS values between the CIR measured at time t and those measured at

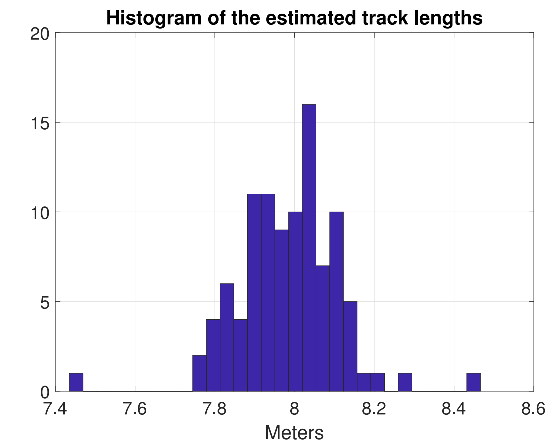

Fig. 11. Histogram of the estimated track lengths for a total of 100 experiments.

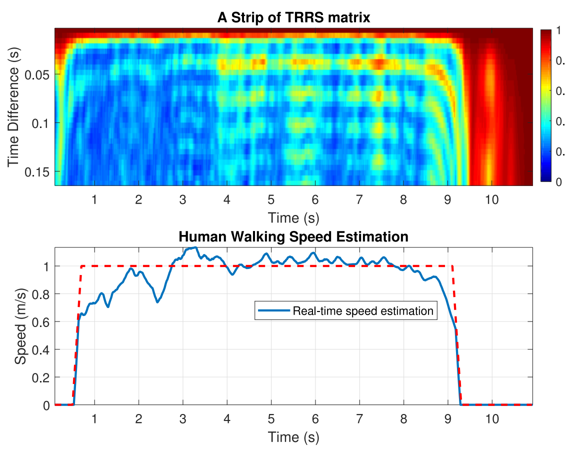

(a)

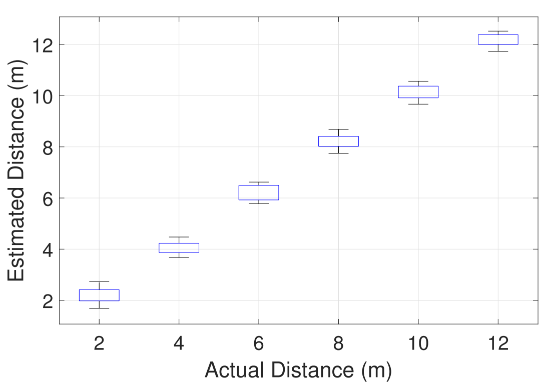

(b)

Fig. 12. Human walking speed/distance estimation. (a) Speed estimation for a controlled human walking speed (1m/s). (b) Results for walking distance estimation.

time $t - \Delta t$, where $\Delta t \in (0\ \text{s}, 0.16\ \text{s}]$, are plotted along the vertical axis. As we can see from the figure, when the person moves slowly (e.g., at the beginning or the end of the experiment), the time differences between the local peaks of the measured TRRS distribution along the vertical axis are greater than that when the person moves faster. In addition, for $t \in [0.5\ \text{s}, 3.5\ \text{s}]$, the asymmetric part of the density function $P(\theta)$ of the energy of MPCs is more significant compared to the case when $t \in [3\ \text{s}, 9.5\ \text{s}]$ and thus the pattern of $J^2(kd)$ is less obvious than the latter one. The bottom panel of Fig. 12(a) shows the corresponding walking speed estimation. The actual distance is 8 m and the estimated walking distance is 7.65 m, so the corresponding error is 4.4%. The loss of performance is from the blockage of signals by the human body, which reduces the number of significant MPCs.

We further let the participant carry the RX and walk for a distance of 2 m, 4 m, 6 m, 8 m, 10 m, and 12 m, respectively. The ground-truth travel distances are measured by a laser distance meter. For each ground-truth distance, the experiment is repeated 20 times with different paths and the walking speed does not need to be constant. The results are shown in Fig. 12(b), where the 5, 25, 75, and 95th percentiles of the estimated distances for each actual distance are plotted from the bottom line to the top line for each block. We find that when the ground-truth distance is small, the error tends to be large. This is mainly because the participant could introduce additional sources of errors which are uncontrollable, such as not following the path strictly, shaking during walking, and not stopping at the exact point in the end. When the distance is short, the impact of this kind of error can be magnified greatly. However, when the walking distance is large, the impact of the uncontrollable errors on the estimation result is insignificant.

B. Estimated Traces in Different Environment

We evaluate the performance of indoor tracking using WiBall in two sets of experiments. In the first set of experiments, a participant walks inside a building with a large open space. He carriers the RX with him and walks from point A on the second floor to point B on the first floor, as shown in Fig. 13(a). The TX is placed closed to the middle of the path on the second floor. The dimension of the building is around $94\,\text{m} \times 73\,\text{m}$. Although the moving distance of the first segment of the path is overestimated, the estimated path is corrected when the participant enters the staircase leading to the first floor.

In the second set of experiments, the participant walks inside an office environment. Fig. 13(b) demonstrates a typical example of the estimated traces in a typical office of a multistory. One RX is put on a cart and the participant pushes the cart along the route from point A to point B, as illustrated in the figure. The dimension of the environment is around $36.3\,\text{m} \times 19\,\text{m}$ and the placement of the TX is also shown in the figure. As we can see from the figure, the estimated path matches the ground truth path very well because the cumulative errors have been corrected by the constraints from the floorplan.

C. Statistical Analysis of Localization Error

To evaluate the distribution of the localization errors, extensive experiments have been conducted in the same office environment shown in Fig. 13(b). The participant pushes the cart with the RX on the cart, following the route as shown in Fig. 14.

The RX starts from Point A and stops at different locations in the route shown in Fig. 14. The lengths of the chosen paths

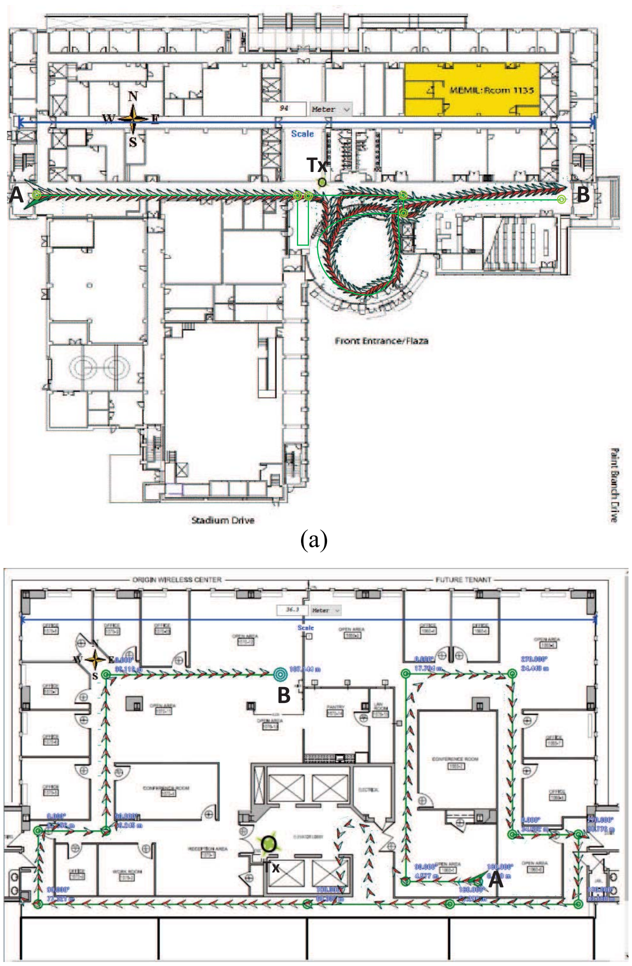

(a)

(b)

Fig. 13. Experiment results in different environments. (a) Estimated path in a building with a lot of open space. (b) Estimated path in an office environment.

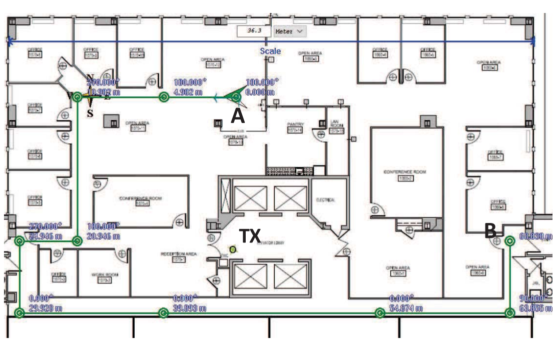

Fig. 14. Route for the evaluation of statistical errors.

are 5, 21, 25, 30, 40, 64, and 69 m, respectively, and the end of each path is marked with two green circles. For each specific path, the experiment is repeated for 25 times. The estimation error for different paths has been analyzed through empirical cumulative distribution function, as shown in Fig. 15. Based on the results, the median of the estimation error for the selected paths is around 0.33 m, and the 80 percentile of the estimation error is within 1 m. Therefore, WiBall is able to achieve a submeter median error in this complex indoor environment.

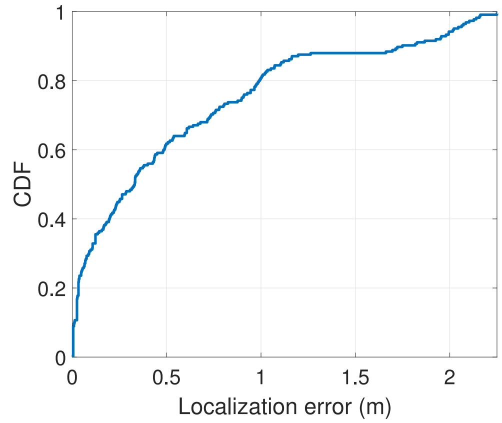

Fig. 15. Empirical CDF of localization error.

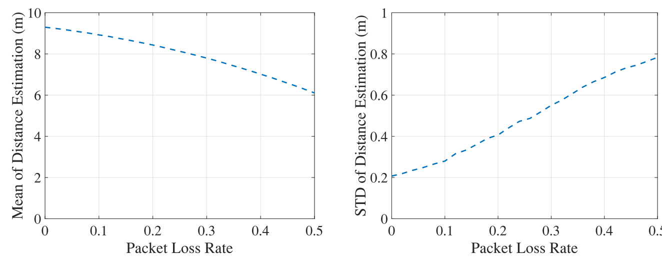

(a) (b)

Fig. 16. Impact of packet loss on the accuracy of distance estimation. (a) Sample mean of the distance estimation. (b) Standard deviation of the distance estimation.

D. Impact of Packet Loss on Distance Estimation

In the previous experiments, WiBall operates on a vacant band and the packet loss rate can thus be neglected. However, in practice, the RF interference from other RF devices operated on the same frequency band will increase the packet loss rate. Since WiBall relies on the first peak of the TRRS distribution for distance estimation, enough samples need to be collected so as to estimate the first peak accurately, and a high packet loss can affect the peak estimation and thus increase distance estimation error.

To study the impact of RF interference, a pair of RF devices is configured to operate in the same frequency band of WiBall to act as an interference source, and we run the tracking system for 100 times with the ground-truth distance being 10 m. When the interfering devices are placed closer to the transmission pair of WiBall, WiBall encounters a higher packet loss rate. Therefore, to obtain various packet loss rates, the interfering devices are placed at different locations during the experiment. The average estimated distance and standard deviation of the estimation under different packet loss rates are shown in Fig. 16. It is seen that a large packet loss rate would lead to an underestimation of the moving distance and increase the deviations of the estimates.

E. Impact of Window Length on Distance Estimation

In the following, the impact of window length on the performance of the proposed TR-based distance estimator is studied. One implicit assumption of the proposed estimator

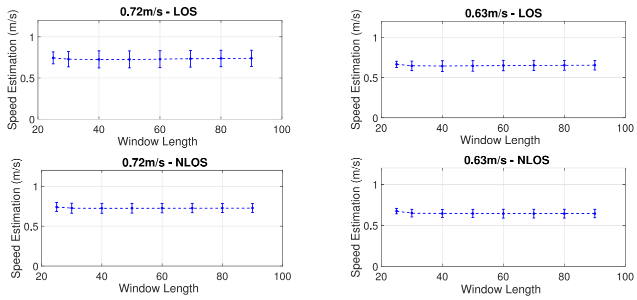

Fig. 17. Impact of window length in terms of speed estimations.

is that the speed of the moving device is constant within the observation window of channel measurements. The length of the observation window should be at least 0.61 λ/v, where v is the actual speed of the device. Furthermore, more samples of channel measurements will also improve the accuracy of $\hat{t}$ as described in Section III-D. Therefore, the window length is an important system parameter of WiBall.

In the following experiments, one RX is put on a toy train whose speed can be tuned and remains constant during each experiment. One TX is placed in two different locations: 1) an LOS location where the RX is within the fields of vision of the TX and 2) an NLOS location where the direct path between the RX and TX is blocked by walls. The TX keeps transmitting packets with a uniform interval of 5 ms. Two experiments are conducted for each location of the TX with two different speeds of the toy train, 0.72 m/s and 0.63 m/s, respectively, and each experiment lasts 10 min. The 5th and 95th percentiles and the sample mean of the estimated speed have been shown in Fig. 17 with different window lengths. It can be observed that when the window length is smaller than 30 samples, the speed estimates have a bias for the both cases; when the window length is greater or equal to 30 samples, the bias is close to 0 and the range of the estimates becomes stable. In addition, a higher accuracy can be achieved when the TX is placed in the NLOS location.

VI. Conclusion

In this paper, we propose WiBall, which offers an accurate, low-cost, calibration-free, and robust solution for INIP in indoor environments without requiring any infrastructure. WiBall leverages the physical properties of the TR focusing ball in radio signals, such as WiFi, LTE, 5G, etc., to estimate the moving distance of an object being monitored and does not need any specialized hardware. It is shown through extensive experiments that WiBall can achieve a decimeter-level accuracy. WiBall is also easily scalable and can accommodate a large number of users with only a single access point or TX. Therefore, WiBall can be a very promising candidate for future indoor tracking systems.

References

[1] (2017). *Global Indoor Positioning and Indoor Navigation (IPIN) Market 2017-2021*. Accessed: Dec. 07, 2017, [Online]. Available: https://tinyurl.com/ya35sh2z

[2] C. Chen, Y. Chen, Y. Han, H.-Q. Lai, and K. J. R. Liu, "Achieving centimeter-accuracy indoor localization on WiFi platforms: A frequency hopping approach," *IEEE Internet Things J.*, vol. 4, no. 1, pp. 111–121, Feb. 2017.

[3] H. Wang *et al.*, "No need to war-drive: Unsupervised indoor localization," in *Proc. 10th Int. Conf. Mobile Syst. Appl. Services*, 2012, pp. 197–210.

[4] Z. Yang *et al.*, "Mobility increases localizability: A survey on wireless indoor localization using inertial sensors," *ACM Comput. Surveys*, vol. 47, no. 3, p. 54, 2015.

[5] G. Park, D. Hong, and C. Kang, "Level crossing rate estimation with doppler adaptive noise suppression technique in frequency domain," in *Proc. IEEE 58th Veh. Technol. Conf. VTC Fall*, vol. 2. Orlando, FL, USA, 2003, pp. 1192–1195.

[6] A. Sampath and J. M. Holtzman, "Estimation of maximum doppler frequency for handoff decisions," in *Proc. 43rd IEEE Veh. Technol. Conf.*, Secaucus, NJ, USA, 1993, pp. 859–862.

[7] C. Xiao, K. D. Mann, and J. C. Olivier, "Mobile speed estimation for TDMA-based hierarchical cellular systems," *IEEE Trans. Veh. Technol.*, vol. 50, no. 4, pp. 981–991, Jul. 2001.

[8] R. Narasimhan and D. C. Cox, "Speed estimation in wireless systems using wavelets," *IEEE Trans. Commun.*, vol. 47, no. 9, pp. 1357–1364, Sep. 1999.

[9] G. Lerosey *et al.*, "Time reversal of electromagnetic waves," *Phys. Rev. Lett.*, vol. 92, no. 19, 2004, Art. no. 193904.

[10] B. Wang, Y. Wu, F. Han, Y.-H. Yang, and K. J. R. Liu, "Green wireless communications: A time-reversal paradigm," *IEEE J. Sel. Areas Commun.*, vol. 29, no. 8, pp. 1698–1710, Sep. 2011.

[11] P. Roux, B. Roman, and M. Fink, "Time-reversal in an ultrasonic waveguide," *Appl. Phys. Lett.*, vol. 70, no. 14, pp. 1811–1813, 1997.

[12] M. Werner, M. Kessel, and C. Marouane, "Indoor positioning using smartphone camera," in *Proc. Int. Conf. Indoor Position. Indoor Navig. (IPIN)*, 2011, pp. 1–6.

[13] R. Mautz and S. Tilch, "Survey of optical indoor positioning systems," in *Proc. Int. Conf. Indoor Position. Indoor Navig. (IPIN)*, 2011, pp. 1–7.

[14] E. M. Gorostiza *et al.*, "Infrared sensor system for mobile-robot positioning in intelligent spaces," *Sensors*, vol. 11, no. 5, pp. 5416–5438, 2011.

[15] I. Rishabh, D. Kimber, and J. Adcock, "Indoor localization using controlled ambient sounds," in *Proc. Int. Conf. Indoor Position. Indoor Navig. (IPIN)*, Sydney, NSW, Australia, 2012, pp. 1–10.

[16] D. K. Barton, *Radar System Analysis and Modeling*, vol. 1. Boston, MA, USA: Artech House, 2004.

[17] L. Shangguan, Z. Yang, A. X. Liu, Z. Zhou, and Y. Liu, "STPP: Spatial-temporal phase profiling-based method for relative RFID tag localization," *IEEE/ACM Trans. Netw.*, vol. 25, no. 1, pp. 596–609, Feb. 2017.

[18] M. Kuhn *et al.*, "High accuracy UWB localization in dense indoor environments," in *Proc. IEEE Int. Conf. Ultra Wideband (ICUWB)*, vol. 2, 2008, pp. 129–132.

[19] J.-Y. Lee and R. A. Scholtz, "Ranging in a dense multipath environment using an UWB radio link," *IEEE J. Sel. Areas Commun.*, vol. 20, no. 9, pp. 1677–1683, Dec. 2002.

[20] D. Giustiniano and S. Mangold, "CAESAR: Carrier sense-based ranging in off-the-shelf 802.11 wireless LAN," in *Proc. 7th Conf. Emerg. Netw. Exp. Technol.*, 2011, p. 10.

[21] S. Sen, D. Kim, S. Laroche, K.-H. Kim, and J. Lee, "Bringing CUPID indoor positioning system to practice," in *Proc. 24th Int. Conf. World Wide Web*, 2015, pp. 938–948.

[22] P. Bahl and V. N. Padmanabhan, "RADAR: An in-building RF-based user location and tracking system," in *Proc. 19th Annu. Joint Conf. IEEE Comput. Commun. Soc. (INFOCOM)*, vol. 2, 2000, pp. 775–784.

[23] Y. Xie, Z. Li, and M. Li, "Precise power delay profiling with commodity WiFi," in *Proc. 21st Annu. Int. Conf. Mobile Comput. Netw.*, 2015, pp. 53–64.

[24] M. Kotaru, K. Joshi, D. Bharadia, and S. Katti, "SpotFi: Decimeter level localization using WiFi," *ACM SIGCOMM Comput. Commun. Rev.*, vol. 45, no. 4, pp. 269–282, 2015.

[25] J. Gjengset, J. Xiong, G. McPhillips, and K. Jamieson, "Phaser: Enabling phased array signal processing on commodity WiFi access points," in *Proc. 20th Annu. Int. Conf. Mobile Comput. Netw.*, 2014, pp. 153–164.

[26] S. Sen, J. Lee, K.-H. Kim, and P. Congdon, "Avoiding multipath to revive inbuilding WiFi localization," in *Proc. 11th Annu. Int. Conf. Mobile Syst. Appl. Services*, 2013, pp. 249–262.

[27] M. Youssef and A. Agrawala, "The Horus WLAN location determination system," in *Proc. 3rd Int. Conf. Mobile Syst. Appl. Services*, 2005, pp. 205–218.

[28] J. Xiong, K. Sundaresan, and K. Jamieson, "ToneTrack: Leveraging frequency-agile radios for time-based indoor wireless localization," in *Proc. 21st Annu. Int. Conf. Mobile Comput. Netw.*, 2015, pp. 537–549.

[29] S. A. Golden and S. S. Bateman, "Sensor measurements for Wi-Fi location with emphasis on time-of-arrival ranging," *IEEE Trans. Mobile Comput.*, vol. 6, no. 10, pp. 1185–1198, Oct. 2007.

[30] K. Qian, C. Wu, Z. Yang, Y. Liu, and K. Jamieson, "Widar: Decimeter-level passive tracking via velocity monitoring with commodity Wi-Fi," in *Proc. 18th ACM Int. Symp. Mobile Ad Hoc Netw. Comput.*, 2017, p. 6.

[31] K. Qian *et al.*, "Widar2.0: Passive human tracking with a single Wi-Fi link," in *Proc. ACM MobiSys*, 2018, pp. 350–361.

[32] P. Castro, P. Chiu, T. Kremenek, and R. Muntz, "A probabilistic room location service for wireless networked environments," in *Ubicomp 2001: Ubiquitous Computing*. Atlanta, GA, USA: Springer, 2001, pp. 18–34.

[33] X. Wang, L. Gao, S. Mao, and S. Pandey, "DeepFi: Deep learning for indoor fingerprinting using channel state information," in *Proc. IEEE Wireless Commun. Netw. Conf. (WCNC)*, New Orleans, LA, USA, 2015, pp. 1666–1671.

[34] X. Wang, L. Gao, and S. Mao, "PhaseFi: Phase fingerprinting for indoor localization with a deep learning approach," in *Proc. IEEE Glob. Commun. Conf. (GLOBECOM)*, San Diego, CA, USA, 2015, pp. 1–6.

[35] Z.-H. Wu, Y. Han, Y. Chen, and K. J. R. Liu, "A time-reversal paradigm for indoor positioning system," *IEEE Trans. Veh. Technol.*, vol. 64, no. 4, pp. 1331–1339, Apr. 2015.

[36] J. Xiong and K. Jamieson, "Arraytrack: A fine-grained indoor location system," in *Proc. USENIX*, 2013, pp. 71–84.

[37] K. Wu *et al.*, "CSI-based indoor localization," *IEEE Trans. Parallel Distrib. Syst.*, vol. 24, no. 7, pp. 1300–1309, Jul. 2013.

[38] S. Sen, R. R. Choudhury, B. Radunovic, and T. Minka, "Precise indoor localization using PHY layer information," in *Proc. 9th Int. Conf. Mobile Syst. Appl. Services*, 2011, pp. 413–414.

[39] H. El-Sallabi, P. Kyritsi, A. Paulraj, and G. Papanicolaou, "Experimental investigation on time reversal precoding for space–time focusing in wireless communications," *IEEE Trans. Instrum. Meas.*, vol. 59, no. 6, pp. 1537–1543, Jun. 2010.

[40] F. Zhang, C. Chen, B. Wang, H.-Q. Lai, and K. J. R. Liu, "A time-reversal spatial hardening effect for indoor speed estimation," in *Proc. IEEE ICASSP*, New Orleans, LA, USA, Mar. 2017, pp. 5955–5959.

[41] Q. Xu, Y. Chen, and K. J. R. Liu, "Combating strong–weak spatial–temporal resonances in time-reversal uplinks," *IEEE Trans. Wireless Commun.*, vol. 15, no. 1, pp. 568–580, Jan. 2016.

Feng Zhang (S'12) received the B.S. and M.S. degrees from the Department of Electronic Engineering and Information Science, University of Science and Technology of China, Hefei, China, in 2011 and 2014, respectively. He is currently pursuing the Ph.D. degree at the Department of Electrical and Computer Engineering, University of Maryland at College Park, College Park, MD, USA.

His current research interests include wireless sensing, statistical signal processing, and wireless indoor localization.

Mr. Zhang was a recipient of the Distinguished TA Award from the University of Maryland at College Park the State Scholarship from the University of Science and Technology of China.

Chen Chen (S'15) received the B.S. and M.S. degrees from the Department of Microelectronics, Fudan University, Shanghai, China, in 2010 and 2013, respectively, and the Ph.D. degree from the Department of Electrical and Computer Engineering, University of Maryland College Park at College Park, College Park, MD, USA in 2017.

He was with Origin Wireless, Inc., Greenbelt, MD, USA. He is currently with Pinterest, Inc., San Francisco, CA, USA.

Dr. Chen was a recipient of multiple honors and awards, including the Chinese Government Award for Outstanding Students Abroad in 2017, the Best Student Paper Award of IEEE ICASSP 2016, the Litton Industries Fellowship from the University of Maryland at College Park in 2015, the Distinguished Graduate Student Teaching Award from the University of Maryland at College Park in 2014, and the Excellent Graduate Student of Shanghai in 2013.

Beibei Wang (SM'15) received the B.S. degree (Highest Hons.) in electrical engineering from the University of Science and Technology of China, Hefei, China, in 2004, and the Ph.D. degree in electrical engineering from the University of Maryland at College Park, College Park, MD, USA, in 2009.

She was with the University of Maryland at College Park, as a Research Associate from 2009 to 2010, and with Qualcomm Research and Development, San Diego, CA, USA, from 2010 to 2014. Since 2015, she has been with Origin Wireless Inc., Greenbelt, MD, USA, where she is currently a Chief Scientist. She coauthored *Cognitive Radio Networking and Security: A Game-Theoretic View* (Cambridge Univ. Press, 2010). Her current research interests include wireless communications and signal processing.

Dr. Wang was a recipient of the Graduate School Fellowship, the Future Faculty Fellowship, the Dean's Doctoral Research Award from the University of Maryland at College Park, and the Overview Paper Award from the IEEE Signal Processing Society in 2015.

Hung-Quoc (Quoc) Lai received the B.S. (*cum laude*), M.S., and Ph.D. degrees from the University of Maryland at College Park, College Park, MD, USA, in 2004, 2006, and 2011, respectively, all in electrical engineering.

He was a Technical Lead in research and development of multiple-input multiple-output and cooperative communications with U.S. Army RDECOM CERDEC, Aberdeen Proving Ground, MD, USA. In 2013, he joined Origin Wireless, Inc., Greenbelt, MD, USA, where he is a founding member and currently the Vice President of Engineering, which develops advanced time reversal wireless technologies for use in a wide variety of applications of indoor positioning/tracking, monitoring, security, radio human biometrics, wireless power transfer, and 5G communications.

Dr. Lai is a Gates Millennium Scholar.

Yi Han received the B.S. degree (Highest Hons.) in electrical engineering from Zhejiang University, Hangzhou, China, in 2011, and the Ph.D. degree from the Department of Electrical and Computer Engineering, University of Maryland at College Park, College Park, MD, USA, in 2016.

He is currently the Wireless Architect with Origin Wireless, Inc., Greenbelt, MD, USA. His current research interests include wireless communication and signal processing.

Dr. Han was a recipient of the Class A Scholarship from Chu Kochen Honors College, Zhejiang University, in 2008 and the Best Student Paper Award of IEEE ICASSP in 2016.

K. J. Ray Liu (F'03) was named a Distinguished Scholar–Teacher of the University of Maryland at College Park, College Park, MD, USA, in 2007, where he is a Christine Kim Eminent Professor of Information Technology. He leads the Maryland Signals and Information Group, conducting research encompassing broad areas of information and communications technology with a recent focus on wireless AI.

Dr. Liu was a recipient of the 2016 IEEE Leon K. Kirchmayer Award on graduate teaching and mentoring, the IEEE Signal Processing Society 2014 Society Award, the IEEE Signal Processing Society 2009 Technical Achievement Award, the Highly Cited Researcher Award by Web of Science, the 2017 CEATEC Grand Prix Award for his invention of the time-reversal machine by Origin Wireless Inc., teaching and research recognitions from the University of Maryland at College Park, including the University-Level Invention of the Year Award, the College-Level Poole and Kent Senior Faculty Teaching Award, the Outstanding Faculty Research Award, and the Outstanding Faculty Service Award, all from A. James Clark School of Engineering, and over a dozen of Best Paper Awards. He has also served as the Editor-in-Chief of the *IEEE Signal Processing Magazine*. He is the IEEE Technical Activities Vice President-Elect. He was the President of IEEE Signal Processing Society, where he has served as the Vice President (Publications and Board of Governor), and a member of the IEEE Board of Director as the Division IX Director. He is a Fellow of the AAAS.